

# Airgap-less Electric Motor: A Solution for High-Torque Low-Speed Applications

M. Alibeik<sup>1</sup>, O. Nezamuddin<sup>1</sup>, M. Rubin<sup>2</sup>, N. Wheeler<sup>1</sup>, S. Silvestri<sup>3</sup>, and E. C. dos Santos<sup>1</sup>

<sup>1</sup>Department of Electrical and Computer Engineering, IUPUI, Indianapolis, USA

<sup>2</sup>Department of Management and Entrepreneurship Indiana University, Bloomington, USA

<sup>3</sup>Department of Mathematics, IUPUI, Indianapolis, USA

**Abstract**—This paper proposes a new category of electric motors able to generate high torque with reduced volume, i.e., high torque density. Such a new design is denominated as an airgap-less electrical motor since the rotor touches the stator as it spins. Due to its zero airgap, the proposed motor will maximize the generated torque, allowing such type of motors to be competitive in applications where hydraulic motors are prevalent, i.e., low-speed and high-torque requirements. Unlike hydraulic motor systems that face two major problems with their braking system and also with low efficiency due to a large number of energy conversion stages (i.e., motor-pump, hydraulic connections and the hydraulic motor itself), the proposed electric motor converts electrical energy directly to mechanical energy with no extra braking system necessary and with higher efficiency. A proof-of-concept electric motor prototype along with its drive system is built to validate the theoretical assumptions proposed in this paper.

## I. INTRODUCTION

A quarter of the electrical energy globally is consumed by electric motors [1]. Electric motors are one of the first options used to generate mechanical torque in different applications due to their high efficiency. Applications include but not limited to electric and hybrid vehicles, pumping systems, etc. Although electric motors have a significant torque density (i.e., torque per motor volume) for the applications mentioned previously, there are other applications (e.g., cranes and winches) where electric motors are not considered a competitive technology as compared to hydraulic motors due to torque density limitations.

Hydraulic motors are commonly used in industrial and commercial applications for their compact size, high power-to-weight ratio, and reliability. In many cases, these characteristics make it preferable over electric motors, especially when high torque density is a critical requirement [2]- [3]. Although hydraulic systems are widely employed in industrial applications (e.g., cranes and winches), they face two major problems, i.e., (1) remarkably inefficient with efficiencies ranging from 6 to 40% and (2) present a complex braking system [4].

Achieving high-torque density has always been one of the targets while designing electric motors [5], which has inspired new designs as presented in the technical literature [6]. For example, although the high torque generated by switched reluctance motors and motors with partitioned rotor are one of the highest among electric motors, they still do not generate

torque density that is comparable with hydraulic motors. Other examples of non-conventional designs of electrical machines and control strategies proposed by industry and academia include: 1) a dual rotor structure along with a dual excitation [7], 2) an outer rotor hybrid excitation [8], 3) new control strategies proposed in order to enhance the mechanical torque [9], and 4) injection of third harmonic current [10].

This paper proposes an airgap-less electric motor that is designed to generate higher level of torque as compared to other electric motor technologies. By reducing the airgap to zero while the rotor spins, the proposed motor and its drive system will maximize the generated torque, thus allowing electric motors to be competitive in applications where hydraulic motors are prevalent, i.e., low-speed and high-torque requirements. While hydraulic motor systems face problems such as braking systems and low efficiency due to a large number of energy conversion stages, the proposed electric motor converts electrical energy directly to mechanical energy with no extra braking system necessary and with higher efficiency.

## II. AIRGAP-LESS MOTOR OPERATION PRINCIPLE

Traditional electric motors are characterized by the presence of an airgap (either constant or variable), which allows the movable part (rotor) to spin freely. Although the airgap presence is fundamental in creating rotational movement, designers try to minimize its size to maximize internal flux and consequently torque. This new family of motors is based on the principle behind magnetic devices that produce linear force, such as relays with a C-core as shown in Fig. 1.

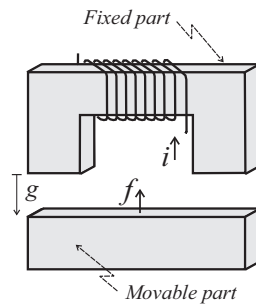


Fig. 1. C-core magnetic device (relay).

Note that the expression for force in this type of device indicates that the attraction observed by the movable part is directly proportional to the current squared ( $i^2$ ), number of turns ( $N$ ), and inversely proportional to the airgap squared ( $g^2$ ), i.e.,  $f = ki^2N/g^2$ ; where  $k$  is a function of the permeability of the material and its dimensions. Hence, the force is maximized if the gap is minimal (i.e., airgap-less), which happens when the movable part touches the fixed one. It is worth mentioning that even using the term airgap-less,  $g$  is not zero due to the roughness of the contact between both parts (movable and fixed). These motors therefore are driven by the concept of airgap-less and maximum attraction force. The proposed motors use physical contact between the stator and rotor to maximize force and rotational torque. Fig. 2 presents different views of a 3D sketch of the proposed motor. Fig. 2(a) shows the stator with 18 poles, Fig. 2(b) presents the rotor. Fig. 2(c) and Fig. 2(d), in turn, highlight both stator and rotor and how the rotor is allowed to touch the stator. The former shows a view in perspective while the latter depicts a top view.

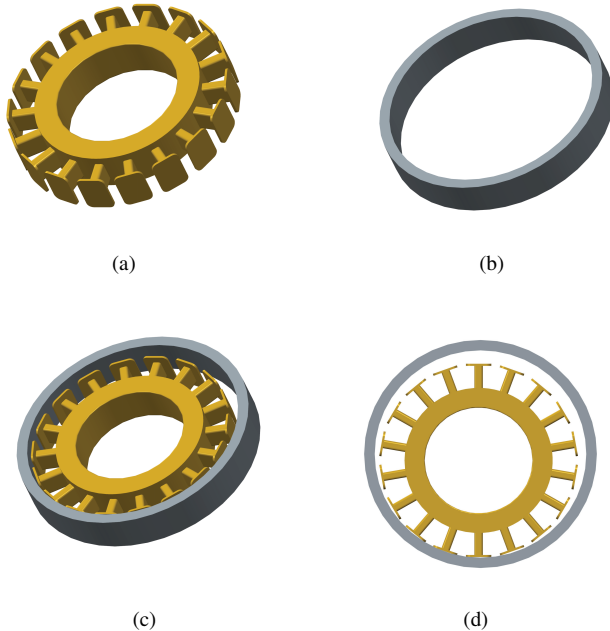


Fig. 2. 3D views of the proposed concept.

The pole excitation signals presented in Fig. 3(b) will guarantee continuous movement of the rotor. These pole excitation signals will be the output of the inverter shown in Fig. 3(a). Fig. 3(c), in turn, shows a sequence of snap shots (top view) that demonstrate how the proposed motor operates. From the left to the right, Fig. 3(c) shows a specific situation where the rotor movement goes counter clock wise. The stator in this motor consists of 18 teeth. The bipole method has been chosen to excite the stator, i.e. every two pole form a pair pole configuration in which one of the teeth are north and the other one is south. As shown in Fig. 3(d), the current will enter a winding in one tooth and leave the winding in the other tooth.

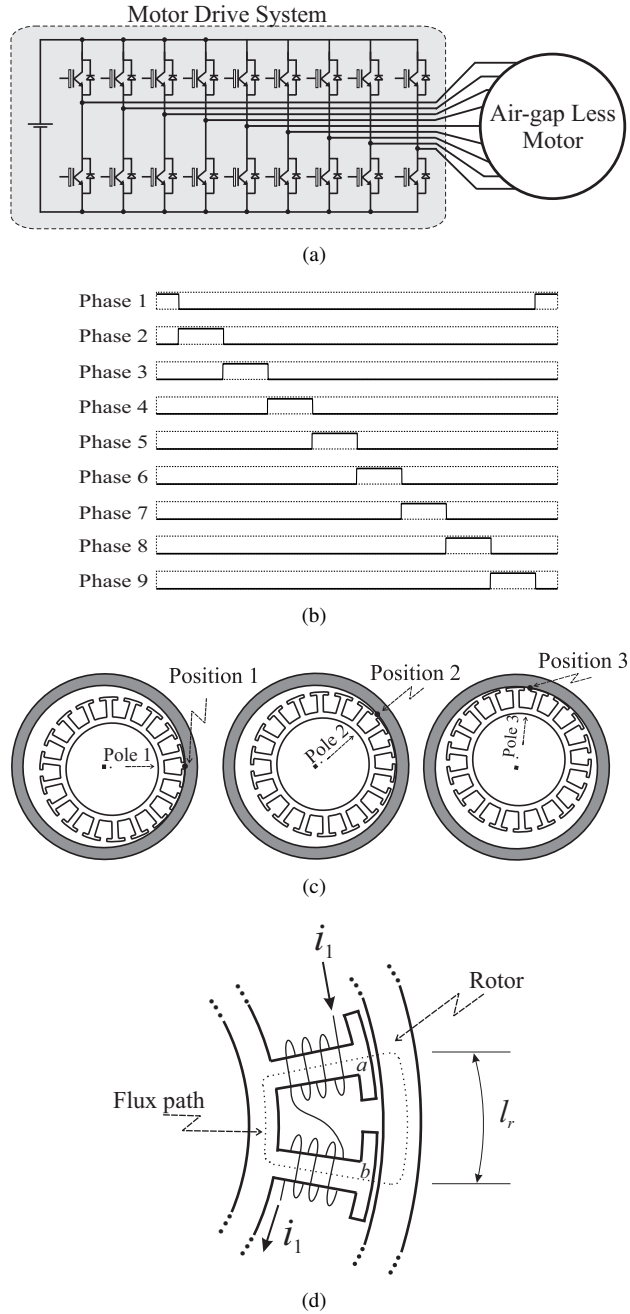


Fig. 3. (a) Location where the winding is placed for MMF creation. (b) Pole excitation Signals. (c) Sequence of shots showing a continuous rotor movement. (d) Bipole configuration

It is noteworthy to mention, the rotation created by this motor is similar to that by hydraulic motors [11], as seen in Fig. 4. Both types of motors (the proposed airgap-less electric motor and the hydraulic motor) have a rigid body rotor with combined translational and rotational movements. Fig. 5(a) presents the trajectory of the rotor center of the proposed motor and how the rotor movement can be obtained by a combination of rotational and translational movements. A mechanical gear can be used to convert this combined translational and rota-

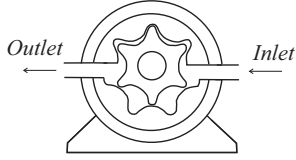


Fig. 4. Hydraulic motor.

tional movement into a rotational movement only if necessary for a specific application [see Fig. 5(b)]. This type of gear box is also used in hydraulic motors.

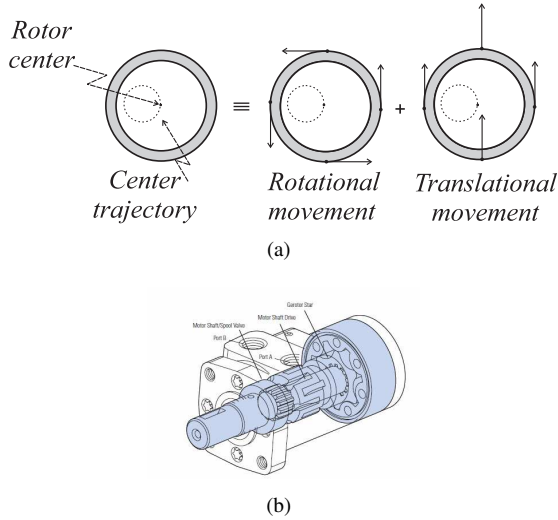


Fig. 5. (a) Combined rotor translational and rotational movements. (b) Gear box.

### III. MOTOR MODELING

As the rotor spins following the stator pole excitation, its center spans a circle as described in Fig. 5(a). Due to this movement, the gap between the stator and rotor changes as a function of the angular position of the rotor  $\theta$ . The flux travels in a path that is normal to both the stator and the rotor, and with this geometric configuration, it is expected to fringe slightly. To simplify the initial derivation, only a path normal to the stator was considered, which is reasonable if the radius of the rotor is close to the radius of the stator. Notice from Fig. 6 that the air gap expression [ $g(\theta)$ ] can be written as a function of angular mechanical position  $\theta$ . The expression for the gap can therefore be derived as shown below:

$$g(\theta) = r_2 - r_{21} \cos(\theta) - \sqrt{r_1^2 - r_{21}^2 \sin^2(\theta)} \quad (1)$$

where  $r_1$ ,  $r_2$ , and  $r_{21}$  are the radii of the stator, rotor, and the difference between both radii (i.e.,  $r_{21} = r_2 - r_1$ ), respectively. In this motor it has been assumed that the radius of the rotor and stator are close to each other, i.e.  $r_1 \approx r_2$ . Considering this assumption, (1) can be written as follows:

$$g(\theta) = r_{21}[1 - \cos(\theta)] \quad (2)$$

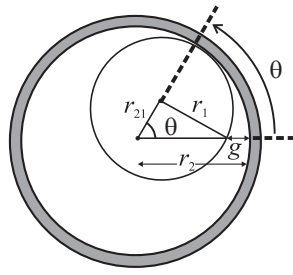


Fig. 6. Geometric approach used for air gap derivation.

Notice that (1) is the gap seen by pole 1 when the rotor is at the mechanical position  $\theta$ , as shown in Fig. 6. There are a total of 9 poles and therefore 9 airgaps of interest (as shown in Fig. 7) which can be defined generally as:

$$g_n(\theta) = 2r_{21}[1 - \cos(\theta - \frac{2\pi(n-1)}{9})] \quad (3)$$

in which  $n$  is the pole number that describes the position of the rotor, i.e. an integer number from 1 to 9. Fig. 7(a) and Fig. 7(b) show two different positions of the rotor in which gaps  $g_2$  and  $g_3$  are approximately zero and gaps  $g_6$  and  $g_7$  are approximately zero, respectively.

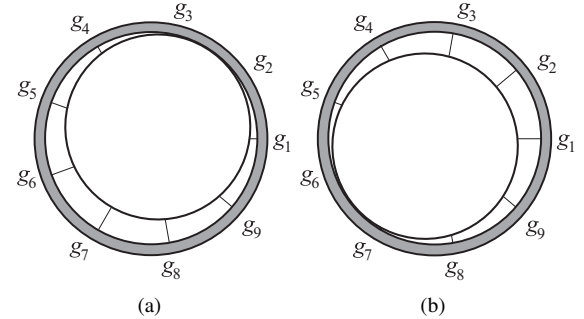


Fig. 7. (a) Rotor position in which gaps  $g_2 \approx g_3 \approx 0$ . (b) Rotor position in which gaps  $g_6 \approx g_7 \approx 0$ .

The magnetic equivalent circuit when only one pole is supplied with current can be modeled as shown in Fig. 8, where  $R_s$ ,  $R_r$ , and  $R_g$  are the reluctances of the stator, rotor, and gap, respectively. It is worth mentioning that when there is no overlap in the pole excitation signals as shown in Fig. 3(b), there will not exist any mutual component in the inductance of each pole and therefore there is only the self component. The total reluctance seen by each pole is therefore given by:

$$R_n = 2R_g + R_s + R_r \quad (4)$$

Each reluctance in (4) is calculated as follows:

$$R_g = g_n(\theta)/\mu_0 A_s \quad (5)$$

$$R_r = l_r/\mu_r A_r \quad (6)$$

$$R_s = l_s/\mu_s A_s \quad (7)$$

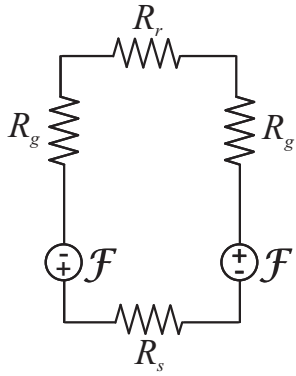


Fig. 8. Magnetic equivalent circuit of the proposed motor when only one pole is supplied with current.

where  $\mu_0$  is the permeability of air,  $A_g$  is the airgap surface area,  $l_r$  is the length of the flux path in the rotor as shown in Fig. 3(d),  $\mu_r$  is the permeability of the rotor,  $A_r$  is the surface area of the rotor (seen by the flux line),  $l_s$  is the length of the flux path in the stator which is the path from point  $a$  to point  $b$  passing through the stator poles as shown in Fig. 3(d),  $\mu_s$  is the permeability of the stator, and  $A_s$  is the surface area of the stator (seen by the flux line).

Substituting (5)-(7) in (4), the total reluctance in the flux path can be found in Fig. 3(d). Once the total reluctances are calculated, (8) can be used to calculate the self inductance at each pole pair:

$$L_n = 2N^2/R_n, \quad \text{with } n = 1, 2, \dots, 9 \quad (8)$$

where  $N$  is the number of turns in the winding.

The inductance for each phase will then be defined as shown below:

$$L_n = \frac{2N^2\mu_0\mu_s\mu_rA_rA_s}{2g_n(\theta)\mu_s\mu_rA_r + l_s\mu_0\mu_rA_r + \mu_0\mu_sA_s l_r} \quad (9)$$

The voltage across each phase can be calculated using:

$$v_n = r_n i_n + L_n \frac{di_n}{dt} \quad (10)$$

in which  $r_n$  is the series resistance in each inductor. Therefore the current through each phase can be calculated from (10) using an integration method.

Once the current in each phase is defined as well as the self inductance, the coenergy in each phase can be derived as shown below:

$$W_{cn} = \frac{1}{2}L_n i_n^2 \quad (11)$$

Using (9) and the current calculated from (10) in (11), the coenergy is then given by:

$$W_{cn} = \frac{i_n^2 N^2 \mu_0 \mu_s \mu_r A_r A_s}{2g_n(\theta) \mu_s \mu_r A_r + l_s \mu_0 \mu_r A_r + \mu_0 \mu_s A_s l_r} \quad (12)$$

The total coenergy in this motor can be calculated as:

$$W_c = \sum_{n=1}^9 W_{cn} \quad (13)$$

After calculating the total coenergy in (13), (14) can be used to calculate the total electrical torque of this motor:

$$T_e = \frac{\partial W_c}{\partial \theta} \quad (14)$$

It is evident from (13) that each phase will contribute to the torque equation as shown below:

$$T_e = \sum_{n=1}^9 T_{en} \quad (15)$$

The torque in each phase will then be calculated using:

$$T_{en} = \frac{\partial W_{cn}}{\partial \theta} \quad (16)$$

Using (12) in (16) the phase torque can be written as a function of the magnetic material employed in both stator and rotor, physical dimensions of the motor, number of turns and mechanical position:

$$T_{en} = \frac{2r_{21}\mu_r^2\mu_s^2\mu_0 A_r^2 A_s N^2 i_n^2 \sin(\theta - \frac{2\pi(n-1)}{9})}{K^2} \quad (17)$$

with,

$$K = [2r_{21}[1 - \cos(\theta - \frac{2\pi(n-1)}{9})]\mu_r\mu_s A_r + l_r\mu_0\mu_s A_s + l_s\mu_0\mu_r A_r] \quad (18)$$

Fig. 9 shows the variation of the peak torque when the relative permeability of the material and number of winding turns change. As expected, the peak torque increases when the number of turns and relative permeability of the material increases. The permeability is the same for both rotor and stator.

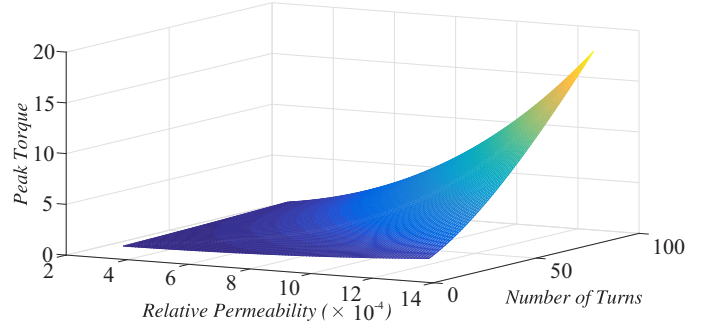


Fig. 9. Variation of the peak torque versus the relative permeability and number of turns.

#### IV. MECHANICAL SPEED AND POSITION

The physical dimensions of the stator and rotor (i.e.,  $r_1$  and  $r_2$ ) will play an important role on how the mechanical speed ( $\omega_m$ ) is related to the electrical angular frequency ( $\omega_e$ ) defined by the nine-leg inverter. To define how much the rotor spins in degrees when the stator excitation completes an entire cycle, consider that position 1 shown in Fig. 10(a) is the initial position of the rotor. After one complete electrical cycle the rotor will be at position 2 shown in Fig. 10(b). From the stator-point-of-view the rotor traveled an angle equal to  $\theta$ .

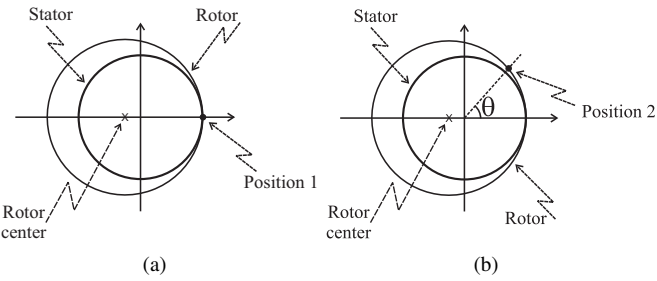


Fig. 10. (a) Initial position of the rotor. (b) Position of the rotor after electrical degrees from stator point of view.

In order to calculate this angle ( $\theta$ ), which can be defined as shown in Fig. 11(a), points  $c$  and  $o$  are defined as rotor center and stator center, respectively.

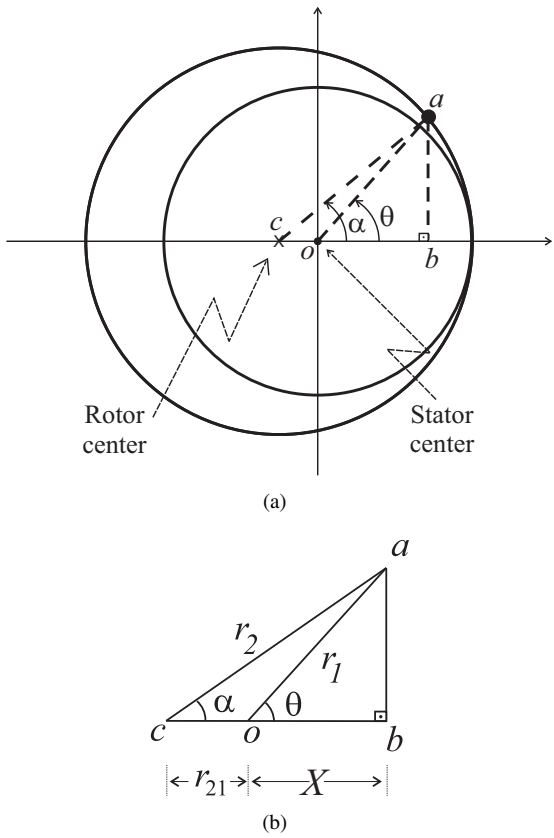


Fig. 11. (a) Position of the rotor after an electrical cycle. (b) Geometrical approach to find angle  $\theta$ .

In Fig. 11(a) the angle  $\alpha$  can be defined as:

$$\alpha = \frac{2\pi r_{21}}{r_2} \quad (18)$$

To find angle  $\theta$ , on the other hand, it is necessary to find the unknown  $X$ , which is the length  $ob$ . From the right triangle  $abc$  in Fig. 11(b):

$$\cos(\alpha) = \frac{r_{21} + X}{r_2} \quad (19)$$

Knowing angle  $\alpha$  from (18), one can find the length  $X$  as following:

$$X = r_2 \cos(\alpha) - r_{21} \quad (20)$$

Considering triangle  $(abo)$ , the angle  $\theta$  can be derived by:

$$\cos(\theta) = \frac{X}{r_1} \rightarrow \theta = \cos^{-1}\left(\frac{X}{r_1}\right) \quad (21)$$

Therefore  $\theta$  is defined as:

$$\theta = \cos^{-1}\left[\frac{r_2 \cos\left(\frac{2\pi r_{21}}{r_2}\right) - r_{21}}{r_1}\right] \quad (22)$$

As it has been stated above, the rotor will travel  $\theta$  radians in one electrical cycle ( $360^\circ$ ). If the electrical frequency is defined as  $f_e = \frac{1}{\tau_e}$ , the electrical speed will be as shown below:

$$\omega_e = 2\pi f_e \quad (23)$$

Note that it will take the same period of time for the rotor to travel  $\theta$  radians, as it takes for one electrical cycle ( $\tau_e$ ), so the mechanical speed can be derived from:

$$\omega_m = \theta f_e \quad (24)$$

from (23) and (24) it is clear that:

$$\frac{\omega_e}{2\pi} = \frac{\omega_m}{\theta} \quad (25)$$

which leads to:

$$\omega_m = \frac{\theta}{2\pi} \omega_e \quad (26)$$

Hence, substituting (22) in (26) the mechanical speed will be defined as shown below:

$$\omega_m = \frac{\cos^{-1}\left[\frac{r_2 \cos\left(\frac{2\pi r_{21}}{r_2}\right) - r_{21}}{r_1}\right]}{2\pi} \omega_e \quad (27)$$

The mechanical speed will increase if the radius of the rotor increases for a given stator radius. It is noteworthy to mention that increasing the mechanical speed with respect to the electrical speed has a limit, as it is shown in Fig. 12. This limit will be reached when the radius of the rotor exceeds 1.45 times the radius of the stator. As it is shown in Fig. 12 the mechanical speed in this motor can reach up to half of the electrical speed as the rotor radius increases.

## V. SIMULATION RESULTS

A MATLAB® code has been written to simulate the proposed motor dynamically. The parameters used in this code are as shown in Table I. Fig. 13 shows the inverter's DC voltage (top waveform) and the inverter's DC current (bottom waveform). Fig. 14 shows the phase voltage (top) and phase current (bottom) for one phase of the stator. As it has been described in the modeling section, phase voltages are generated by the inverter shown in Fig. 3(a).

Fig. 15 shows the torque generated by the proposed motor. The torque ripple can be reduced with: (1) an overlap on the motor voltage applied to each phase and (2) an increase in the number of poles.

TABLE I  
PARAMETERS USED IN THE SIMULATION

Parameter	Description	Value
$B_m$	Coefficient of friction	0.1
$J_m$	Moment of inertia	$0.01 (Kg.m^2)$
$V_{dc}$	DC link voltage	20 (V)
$\mu_0$	Permeability of air	$4\pi \times 10^{-7}(H/m)$
$\mu_s$	Relative Permeability of the stator	2000
$\mu_r$	Relative Permeability of the rotor	700
$l_s$	Length of the flux path in the stator	0.1 (m)
$l_r$	Length of the flux path in the rotor	0.07 (m)
$A_s$	Cross sectional area of the stator	$140 \times 10^{-6}(m^2)$
$A_r$	Cross sectional area of the rotor	$25 \times 10^{-5}(m^2)$
$N$	Number of turns in each tooth	160
$r$	Series resistance in each winding	3 ( $\Omega$ )
$R_s$	Stator radius	0.0953 (m)
$R_r$	Rotor radius	0.096 (m)
$f_e$	Electrical frequency	2 (Hz)

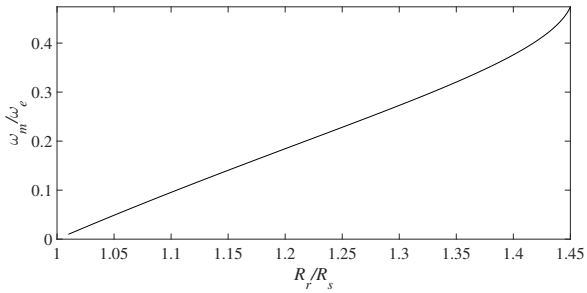


Fig. 12. Mechanical speed and electrical speed ratio vs. radius of rotor and radius of stator ratio.

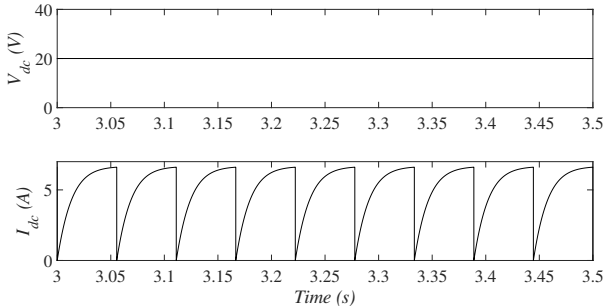


Fig. 13. Input DC voltage (Top). Input DC current (Bottom).

## VI. EXPERIMENTAL SETUP AND RESULTS

A proof-of-concept laboratory prototype was built to validate the theoretical assumptions. The rotor in this prototype is made of low carbon steel 1018 which is shown in Fig. 16(a) and the stator is made of steel M19 shown in Fig. 16(b). Notice that in Fig. 16(b), the stator is not yet wrapped with windings. This stator is consisted of 18 teeth (9 pole pairs). Fig. 17 shows a photo of the proposed motor in perspective

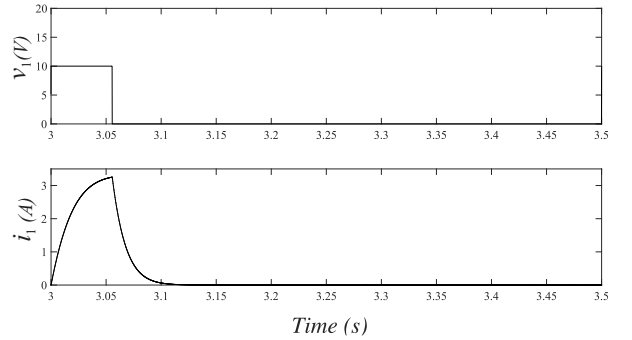


Fig. 14. Voltage of phase 1 (Top). Current of phase 1 (Bottom).

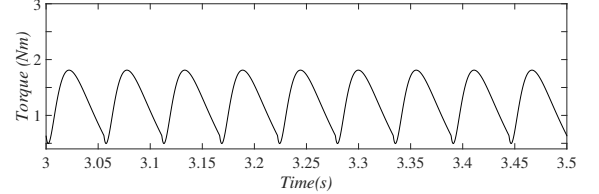


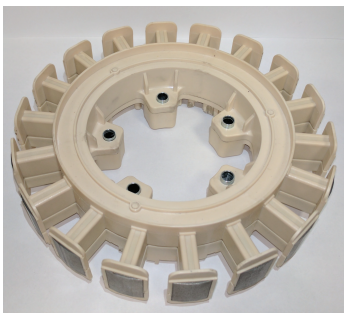
Fig. 15. Electrical torque.

and assembled as a single unit. The entire experimental setup for this prototype including the drive system is presented in Fig. 18. The motor excitation voltages are generated by the inverter as shown schematically in Fig. 3(a). In this experimental setup, the inverter used to generate these voltages is IRAMX20UP60A. This inverter is a 3-leg inverter and since the proposed motor needs nine excitation voltages, three of these inverters have been used in the setup.

A DC voltage of 20V has been supplied to the system through a power supply shown in Fig. 18. Fig. 19 shows the input DC voltage (top waveform) and the input DC current (bottom waveform) of the inverter. Note that this result is in



(a)



(b)

Fig. 16. (a) External rotor. (b) Stator with 18 teeth.



Fig. 17. Proposed motor prototype.

accordance with the simulation result presented in Fig. 13.

The proposed motor has been operated using three different electric frequencies of 2, 5, and 10 Hz as shown in Fig. 20(a), 20(b), and 20(c), respectively. These figures show how the zero mechanical speed torque relates to input electrical power. When the speed is increased, the torque will decrease for the given power. For instance, the torque for the power of 35W is around 3Nm, as it is shown in Fig. 20(a) with the frequency is 2Hz. The same amount of power gives 2.8Nm and 2.6Nm in Fig. 20(b) and 20(c) with the frequencies are 5Hz and 10Hz, respectively.



Fig. 18. Experimental setup.

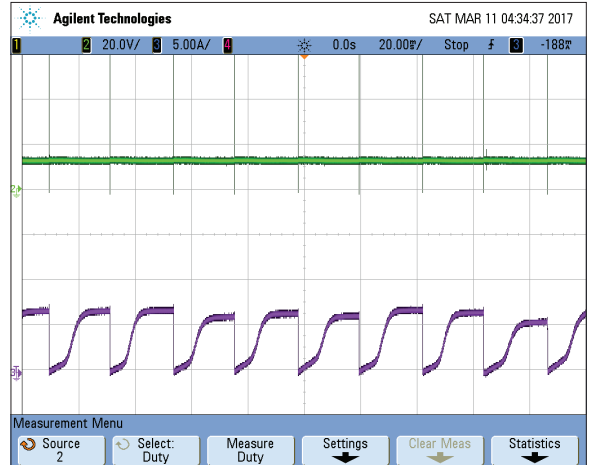
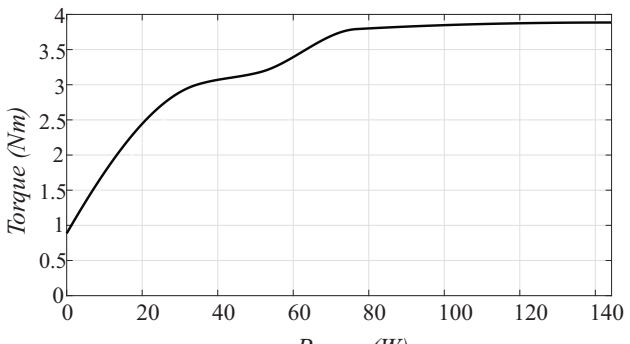


Fig. 19. Input voltage (top waveform) and DC link current (bottom waveform).

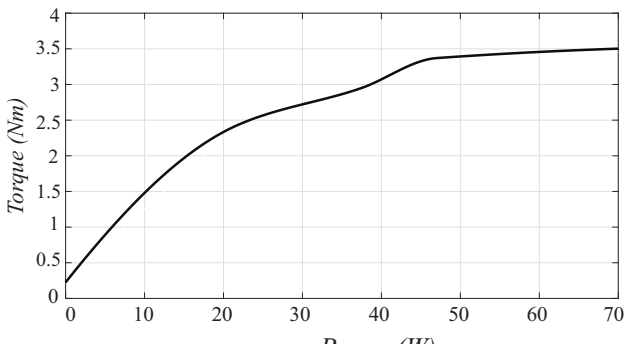
## VII. CONCLUSION

An airgap-less electric motor has been proposed in this paper. This motor is designed to generate higher level of torque as compared to other electric motors. The level of torque in the proposed motor allows it to be comparable to hydraulic motors in low speed high torque applications such as crane, winches, and etc. Unlike the hydraulic motors, this motor converts the electrical energy to the mechanical energy directly which will result in higher level of efficiency. Fig. 21 shows the comparison between torque/mass of 4 different motors: (1) the internal permanent magnet motor [12], (2) inner rotor modulated PSMS [13], (3) airgap-less motor (not optimized), and (4) airgap-less motor (optimized). As it is shown in this figure, the torque of the airgap-less motor (the proposed motor) is approximately  $2.2 \text{Nm/Kg}$ . Notice that this torque has been obtained experimentally from the proposed motor without any optimization in terms of magnetic material and lamination.

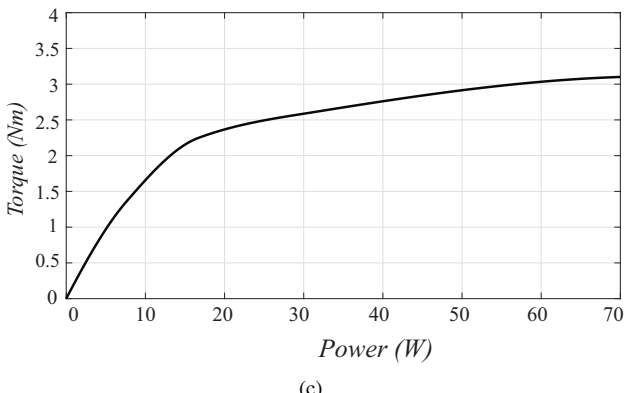
Using different magnetic material (higher permeability) and increasing number of turns result into bigger levels of torque. The peak torque per kilogram can therefore increase to  $5.6 \text{Nm/Kg}$  as expected from Fig. 9 and shown in Fig. 21.



(a)



(b)



(c)

Fig. 20. Torque vs. power using different frequencies: (a) 2Hz. (b) 5Hz. (c) 10Hz.

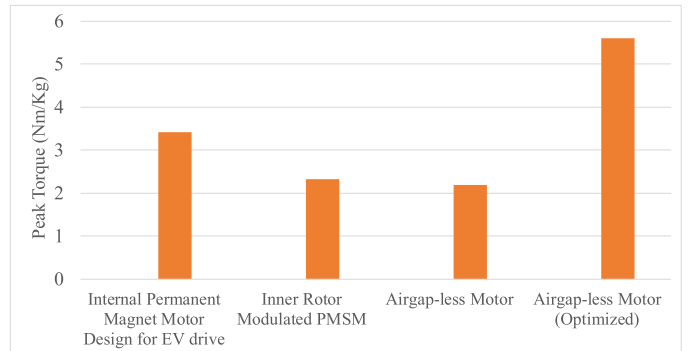


Fig. 21. Comparison between different motors in  $Nm/Kg$ .

*Conference on Electrical Machines - ICEM 2010*, Sept 2010, pp. 1–6.

- [6] P. Rafajdus, A. Peniak, D. Peter, P. Maky, and L. Szab, “Optimization of switched reluctance motor design procedure for electrical vehicles,” in *2014 International Conference on Optimization of Electrical and Electronic Equipment (OPTIM)*, May 2014, pp. 397–404.
- [7] M. Z. Ahmad, E. Sulaiman, Z. A. Haron, and T. Kosaka, “Design improvement of a new outer-rotor hybrid excitation flux switching motor for in-wheel drive ev,” in *2013 IEEE 7th International Power Engineering and Optimization Conference (PEOCO)*, June 2013, pp. 298–303.
- [8] Y. Wang, Z. Zhang, R. Liang, W. Yuan, and Y. Yan, “Torque density improvement of doubly salient electromagnetic machine with asymmetric current control,” *IEEE Transactions on Industrial Electronics*, vol. 63, no. 12, pp. 7434–7443, Dec 2016.
- [9] R. O. C. Lyra and T. A. Lipo, “Torque density improvement in a six-phase induction motor with third harmonic current injection,” *IEEE Transactions on Industry Applications*, vol. 38, no. 5, pp. 1351–1360, Sep 2002.
- [10] J. Lee, “Structural design optimization of electric motors to improve torque performance,” Ph.D. dissertation, Citeseer, 2010.
- [11] Y. Yang, L. Ma, and D. Huang, “Development and repetitive learning control of lower limb exoskeleton driven by electro-hydraulic actuators,” *IEEE Transactions on Industrial Electronics*, vol. PP, no. 99, pp. 1–1, 2016.
- [12] K. I. Laskaris and A. G. Kladas, “Internal permanent magnet motor design for electric vehicle drive,” *IEEE Transactions on Industrial Electronics*, vol. 57, no. 1, pp. 138–145, 2010.
- [13] J. M. Crider and S. D. Sudhoff, “An inner rotor flux-modulated permanent magnet synchronous machine for low-speed high-torque applications,” *IEEE Transactions on Energy Conversion*, vol. 30, no. 3, pp. 1247–1254, Sept 2015.

## REFERENCES

- [1] P. Walde and C. U. Brunner, “Energy-efficiency policy opportunities for electric motor-driven systems,” 2011.
- [2] A. S. Abdel-Khalik, A. M. Massoud, and S. Ahmed, “A senior project-based multiphase motor drive system development,” *IEEE Transactions on Education*, vol. 59, no. 4, pp. 307–318, Nov 2016.
- [3] B. S. Armstrong and Q. Yuan, “Multi-level control of hydraulic gerotor motors and pumps,” in *American Control Conference, 2006*. IEEE, 2006, pp. 8–pp.
- [4] C.-S. Kim and C.-O. Lee, “Speed control of an overcentered variable-displacement hydraulic motor with a load-torque observer,” *Control Engineering Practice*, vol. 4, no. 11, pp. 1563–1570, 1996.
- [5] K. Sato, J. S. Shin, T. Koseki, and Y. Aoyama, “Basic experiments for high-torque, low-speed permanent magnet synchronous motor and a technique for reducing cogging torque,” in *The XIX International*